Earth and Planetary Science Letters 304 (2011) 407–416

Contents lists available at ScienceDirect

Earth and Planetary Science Letters

journal homepage: www.elsevier.com/locate/epsl

Argon diffusion in pyroxenes: Implications for thermochronometry and mantle degassing

William S. Cassata *, Paul R. Renne, David L. Shuster

Department of Earth and Planetary Sciences, University of California-Berkeley, 307 McCone Hall #4767, Berkeley, CA 94720-4767, USA
Berkeley Geochronology Center, 2455 Ridge Road, Berkeley, CA 94709, USA

ARTICLE INFO

Article history:
Received 1 September 2010
Received in revised form 8 February 2011
Accepted 9 February 2011

Editor: R.W. Carlson

Keywords:
diffusion
pyroxene
argon
thermochronometry
mantle
atmosphere

ABSTRACT

The rate at which argon diffuses in pyroxenes is relevant to several problems in the Earth and planetary sciences. Pyroxenes are among the most abundant minerals in the Earth's upper mantle and are important hosts for potassium and radiogenic ^{40}Ar (^{40}Ar*). Additionally, pyroxenes commonly contain >25% of the total ^{40}Ar* within meteorites, and therefore hold great potential for quantifying the timing, duration, and thermal conditions of events experienced by meteorites and their parent bodies. We conducted detailed, feedback-controlled laser heating diffusion experiments using synthetically produced ^{37}Ar in gem-quality clinopyroxene (CPX) and orthopyroxene (OPX) crystals. Stepwise heating between 850 and 1350 °C yielded linear Arrhenius arrays from which activation energies (E_a) of 379.2 ± 4.1 and 371.0 ± 6.0 kJ/mol and pre-exponential factors (D_o) of $(1.36\times10^{-4})^{+1.12\times10^{-4}}_{-6.15\times10^{-5}}$ and $(5.73\times10^{-2})^{+3.72\times10^{-2}}_{-2.25\times10^{-2}}$ were determined for CPX and OPX, respectively; these E_a's are an order of magnitude higher than previously reported values obtained with a different experimental approach (Watson et al., 2007) and indicate that Ar diffusion within pyroxenes is strongly temperature dependent. At high temperatures Ar diffusion in pyroxenes is rapid, which indicates that diffusive ^{40}Ar distributions observed within meteoritic pyroxenes may provide information about brief, high-temperature shock heating events. In contrast, subsequent low-T conditions should minimally influence these concentration gradients. The experimental Ar diffusion kinetics in OPX and CPX correspond to closure temperatures of 600–700 and 700–800 °C, respectively (for 10 °C/Ma cooling). These results suggest that diffusive equilibration through 0.1–0.5 mm pyroxene grains occurs in minutes to hours at basaltic melt generation temperatures (~1300 °C), and is therefore unlikely to inhibit mantle degassing.

1. Introduction

Thermochronometry by the ^{40}Ar/^{39}Ar technique provides insights into an array of Earth and planetary processes, including mountain uplift and erosion (e.g., Richter et al., 1991), pluton emplacement and cooling (e.g., Brownlee and Renne, 2010), regional metamorphism (e.g., Kohn et al., 1995), asteroid accretion and cooling (e.g., Renne, 2000), and shock metamorphism of meteorites and their parent bodies (e.g., Turner et al., 1978). Most studies have utilized K-rich phases such as feldspars, micas, and amphiboles because these minerals are primary carriers of radiogenic ^{40}Ar (^{40}Ar*). As pyroxenes have a low K concentration relative to these phases, they have not been extensively used as thermochronometers, yet they are abundant in Earth's upper mantle and in fragments of other planetary bodies represented by meteorites.

Despite their low K concentration, pyroxenes often contain sufficiently abundant ^{40}Ar* to yield useful geochronologic constraints. Whole-rock ^{40}Ar/^{39}Ar age spectra obtained from various chondritic and Martian meteorites indicate that pyroxenes host up to 10–50% of the total K budget and yield reproducible ages (e.g., Bogard et al., 1995; Cassata et al., 2010; Kunz et al., 1997; Wang et al., 1980). ^{40}Ar/^{39}Ar data have been used to constrain the timing of shock metamorphism and qualitatively assess the thermal conditions that prevailed during these events. Pyroxenes have also been shown to be important carriers of ^{40}Ar* in the Earth's mantle and crust. Clinopyroxene inclusions within diamonds contain up to 1.4 wt.% K (Burgess et al., 1989; Phillips et al., 1989, 2004). These pyroxenes, as well as those in alpine metamorphic complexes (e.g., Haiqing et al., 1996; Wang et al., 2000) and ophiolite sequences (e.g., You, 1997), have been successfully dated by the ^{40}Ar/^{39}Ar technique. To relate these geochronologic constraints to thermal conditions experienced by the host rocks (i.e., a closure temperature or continuous thermal history), the kinetics of Ar diffusion in pyroxenes must be known.

There have been few attempts to quantify diffusion parameters (E_a and D_o) for Ar in pyroxenes using step-wise and bulk degassing experiments. Amirkhanov et al. (1959) first reported an E_a for ^{40}Ar in pyroxene of 307 kJ/mol. Hart (1960) and Fechtig et al. (1960) failed to obtain linear Arrhenius arrays from pyroxene crystals. Schwartzman and Giletti (1977) reported an E_a for ^{40}Ar in pyroxene of >301 kJ/mol.

* Corresponding author.
E-mail addresses: cassata@berkeley.edu (W.S. Cassata), prenne@bgc.org (P.R. Renne), dshuster@bgc.org (D.L. Shuster).

0012-821X/$ – see front matter © 2011 Elsevier B.V. All rights reserved.
doi:10.1016/j.epsl.2011.02.019

Haiqing et al. (1996) reported an E_a for ^{39}Ar in pyroxene of 407 kJ/mol. Several subsequent studies of whole-rock meteorites (e.g., Cassata et al., 2010; Kunz et al., 1997; Weirich et al., 2010) used ^{37}Ar data acquired in step-heating ^{40}Ar/^{39}Ar experiments to quantify diffusion parameters, using the isotopic composition (i.e., $^{39}Ar_K/^{37}Ar_{Ca}$) to distinguish Ar evolved from pyroxenes versus other phases, and inferred comparably high activation energies (300 to 406 kJ/mol). Thus existing *in vacuo* degassing data indicate that Ar diffusion in pyroxenes is more strongly temperature-dependent than in commonly analyzed, higher-K materials. Nonetheless, the reproducibility of Ar diffusion kinetics in pyroxenes and their potential utility for Ar thermochronometry remains relatively unconstrained.

Watson et al. (2007) reported diffusion parameters obtained from Rutherford backscattering (RBS) measurements of experimental Ar-uptake profiles in orthopyroxenes. The concentration profiles, which were restricted to the outermost 50–60 nm of enstatite crystals, led Watson et al. (2007) to infer values of $D_o = 1.4 \times 10^{-20}$ m^2 s^{-1} and $E_a = 32.2$ kJ mol^{-1} for orthopyroxene, and similar values were assumed to apply to clinopyroxene. These diffusion parameters indicate that Ar mobility in pyroxenes is (1) only weakly dependent on temperature, (2) exceedingly slow at magmatic temperatures, and (3) negligible at typical laboratory degassing temperatures and timescales. The dramatic difference between the results of Watson et al. (2007) and the aforementioned *in vacuo* heating experiments, and the important implications of these differences, prompted our further investigation of Ar diffusion in pyroxenes. In this paper we present results of a series of diffusion experiments conducted on individual grains of gem-quality clinopyroxene and orthopyroxene.

2. Sample characterization and selection

Gem-quality orthopyroxene and clinopyroxene crystals were purchased from PrettyRock.com (http://www.prettyrock.com) and are designated PR-OPX and PR-CPX, respectively. The geologic provenance of these pyroxenes is unknown. Composition and homogeneity were evaluated by electron microprobe analysis (EMPA) of polished grain mounts at the University of Oregon CAMCOR facility, using methods described by Renne et al. (2010). Both proved to be homogenous and inclusion-free within analytical precision for the elements analyzed, which included Si, Al, Ti, Fe, Mg, Ca, K, Na, Mn, Cr and Ni. Average compositions are summarized in Table 1 and correspond to $En_{90.5}Fs_{9.3}Wo_{0.2}$ and $En_{49.0}Fs_{1.6}Wo_{49.3}$ for PR-OPX and PR-CPX, with mean CaO concentrations of 0.13 ± 0.02 and 24.61 ± 0.39 wt.%, respectively.

Table 1
Pyroxene compositional data.

	PR-CPX (n = 53)		PR-OPX (n = 84)	
	Ave.	S.D.	Ave.	S.D.
SiO_2	55.03	0.27	57.46	0.22
TiO_2	0.07	0.02	0.04	0.02
Al_2O_3	0.22	0.01	0.10	0.01
Cr_2O_3	0.68	0.04	0.01	0.01
FeO*	1.04	0.03	6.31	0.04
NiO	0.02	0.02	0.01	0.02
MnO	0.05	0.01	0.24	0.02
MgO	17.58	0.13	34.56	0.08
CaO	24.61	0.39	0.13	0.02
Na_2O	0.34	0.03	0.02	0.02
K_2O	0.00	0.00	0.00	0.00
Total	99.65		98.87	
En	49.0		90.5	
Fs	1.6		9.3	
Wo	49.3		0.2	

Equant to elongate tetragonal prisms devoid of fractures and ranging in size from ~300 μm^3 to 1200 μm^3 were selected for analysis. Additionally, two cleavage-bounded sheet-like fragments of CPX with high aspect ratios (>10:5:1) were analyzed to test for diffusive anisotropy normal to the {110} and {100} crystal faces. The lattice orientations of these crystal fragments were determined using backscatter diffraction (EBSD) with a Zeiss EVO scanning electron microscope (SEM) using TSL-OIM software. The dimensions of select grains, including the thin sheets, were measured using a binocular microscope. Photographs of these crystals and their dimensions are given in the supplementary files.

3. Ar diffusion experiments

3.1. Analytical details

Pyroxene crystals were irradiated for 50 to 100 h at the Oregon State University TRIGA reactor in the Cadmium-Lined In-Core Irradiation Tube (CLICIT) facility. Individual crystal fragments were loaded into metal packets made from high purity Pt–Ir tubes and incrementally degassed using feedback-controlled laser heating with a 150 W diode laser ($\lambda = 810 \pm 10$ nm) equipped with a coaxially aligned optical pyrometer [methods described in detail in Cassata et al. (2009) and Shuster et al. (2010)]. To account for the temperature dependent emissivity of the Pt–Ir packets, we calibrated the single-color pyrometer output against a type-K thermocouple under high vacuum (<10^{-8} Torr) and under the same conditions as the diffusion experiments (i.e., same viewport, coverslide, focal point, etc.). Calibrations were conducted between 400 and 1300 °C and upward extrapolation was required to correct higher temperature data (calibration curve appears in the supplementary files). CPX crystals were heated in excess of their nominal melting temperature (1351 °C for pure diopside; Yoder, 1952) and were completely fused following incremental heating. Although OPX crystals were not fused, at temperatures above 1400 °C increasing extraction temperatures and durations resulted in progressively lower gas yields that comprise less than 1% of the total ^{37}Ar (see supplementary files). Data were corrected for mass discrimination, ^{37}Ar decay ($t_{1/2} = 34.95$ days; Renne and Norman, 2001), and extraction line blanks.

3.2. Calculating diffusion coefficients

To quantify diffusion kinetics, we used Ca-derived ^{37}Ar as the diffusant because this synthetically produced isotope has a uniform concentration throughout these compositionally homogeneous pyroxenes and minimal contribution from the procedural blank. Using the fractions of ^{37}Ar degassed and the duration of each step, we calculate the diffusion coefficient (D) normalized to the characteristic length scale (D/a^2) using the equations of Crank (1975) for spherical geometry (for the equant to elongate tetragonal prisms) and infinite sheet geometry (for the oriented slabs) following the algorithm of Fechtig and Kalbitzer (1966). We quantified the temperature dependence (E_a) of the diffusion coefficients from weighted linear regression models of $\ln(D/a^2)$ against $1/T$.

Incremental releases of ^{36}Ar, ^{38}Ar, ^{39}Ar, and ^{40}Ar were also measured. Because potassium is a trace element in these pyroxenes, ^{39}Ar signals were negligibly above the background. Similarly, ^{36}Ar, ^{38}Ar, and ^{40}Ar are present only in minor quantities and may be heterogeneously distributed, and were therefore not used to quantify diffusion kinetics. In discussing the implications of our results, we assume that laboratory-derived ^{37}Ar diffusion parameters reflect the kinetics of radiogenic ^{40}Ar (^{40}Ar*) diffusion in natural settings. Although ^{37}Ar may diffuse slightly more rapidly than ^{40}Ar owing to its lower mass, such mass-dependent phenomena have not been observed in detailed studies of ^{37}Ar and ^{39}Ar diffusion in feldspars (e.g., Cassata et al., 2009). Regardless, any mass-dependent effects, if

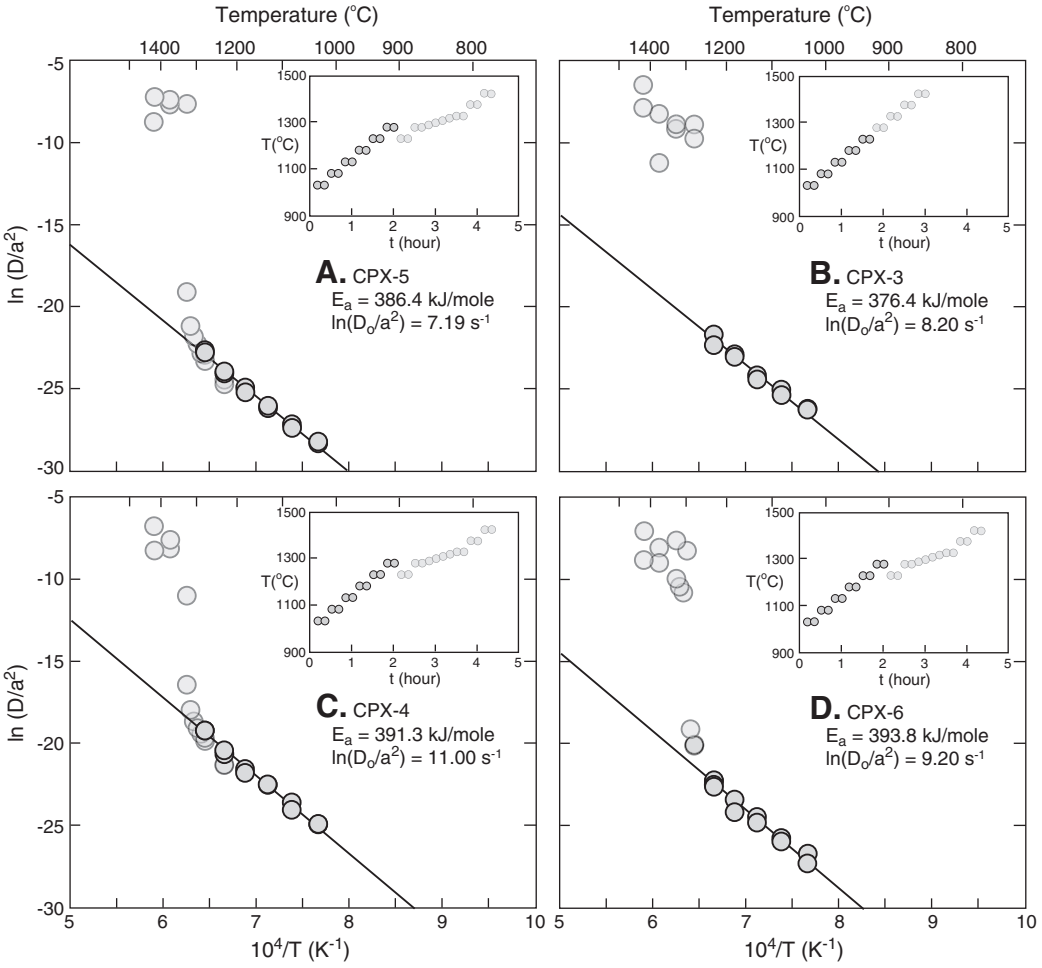

Fig. 1. Arrhenius plots for (A) CPX-5, (B) CPX-3, (C) CPX-4, and (D) CPX-6. Uncertainties in calculated D/a^2 values are generally smaller than the symbols, but are not shown. The laboratory heating schedules are shown in the insets. Data corresponding to lighter symbols were not included in E_a and $\ln(D_o/a^2)$ calculations.

present, would be negligible (e.g., the square root of the ratio of the atomic masses is 1.04).

4. Results

Incremental heating experiments were conducted on gem quality CPX and OPX crystal fragments. Samples were subjected to one of two different types of heating schedules: monotonically increasing temperatures with duplicate isothermal steps or cycled heating with duplicate isothermal steps. In calculating D/a^2 values, cycled and isothermal heating analyses test the assumed initial condition that ^{37}Ar is produced uniformly throughout a single diffusion domain (e.g., Lovera et al., 1991). Complete stepwise degassing data appear in the supplementary files.

Activation energies (E_a) were determined by linear regressions of the maximum number of consecutive low-temperature steps that yielded an MSWD $\leq$2.5 (normally all steps preceding unambiguous departures from linear Arrhenius arrays). In some aliquots the first extraction released an anomalously large abundance of ^{37}Ar, possibly reflecting the degassing of small surficial domains or recoiled ^{37}Ar in addition to structurally bound ^{37}Ar. If this step is included in D/a^2 calculations, then the subsequent two to six steps yield higher than expected D/a^2 values that do not replicate upon isothermal heating. However, when excluded from D/a^2 calculations, the goodness of fit of subsequent extractions is improved (see Supplementary Files Fig. 1). To avoid biasing the results, the low-temperature extractions were excluded if they differed significantly (by more than one natural log unit) from a downward extrapolation of the Arrhenius relationship delineated by subsequent extractions. Data included in E_a calculations were generally acquired between 850 and 1350 °C and define highly reproducible, linear Arrhenius arrays (Figs. 1–3). CPX grains yield an average E_a of 379.2 ± 4.1 kJ/mol (90.6 ± 1.0 kcal/mol) and $\ln(D_o/a^2)$ between 7.2 and 12.4 (Table 2; Fig. 4).[1] OPX grains yield an average E_a of 371.0 ± 6.0 kJ/mol (88.7 ± 1.4 kcal/mol) and $\ln(D_o/a^2)$ between 13.1 and 16.6 (Table 2; Fig. 4). For a 10 °C/Ma cooling rate, these diffusion parameters correspond to closure temperatures of 600 to 700 and 700 to 800 °C for CPX and OPX, respectively (Fig. 4). Some grains (typically the largest) yielded non-linear Arrhenius arrays typical of crystals with multiple diffusion domains (Fig. 5; discussed in greater detail below). These crystals have not been included in E_a and D_o calculations.

Above ~1225 or 1350 °C for CPX and OPX, respectively, the linear Arrhenius arrays we used to quantify E_a terminate abruptly and D/a^2 values increase over a ~50 °C interval to values that are orders of magnitude higher than expected from upward extrapolation of the lower-T linear Arrhenius relationships described above (i.e., the Arrhenius arrays curve sharply upward; Figs. 1–3). Individual OPX and CPX fragments lost between 15 and 25% and 0.1 and 1.0%, respectively, of the total ^{37}Ar prior to departures from linear Arrhenius arrays (Table 2). Because these OPX and CPX fragments were taken from larger, homogeneous, gem-quality pyroxenes, each is expected to have the

[1] Calculated E_a's are marginally dependent upon the assumed diffusion geometry (spherical) when more than ~15% of the total gas is included in the regression, and may overestimate the true E_a by up to ~5% (Huber et al., 2011).

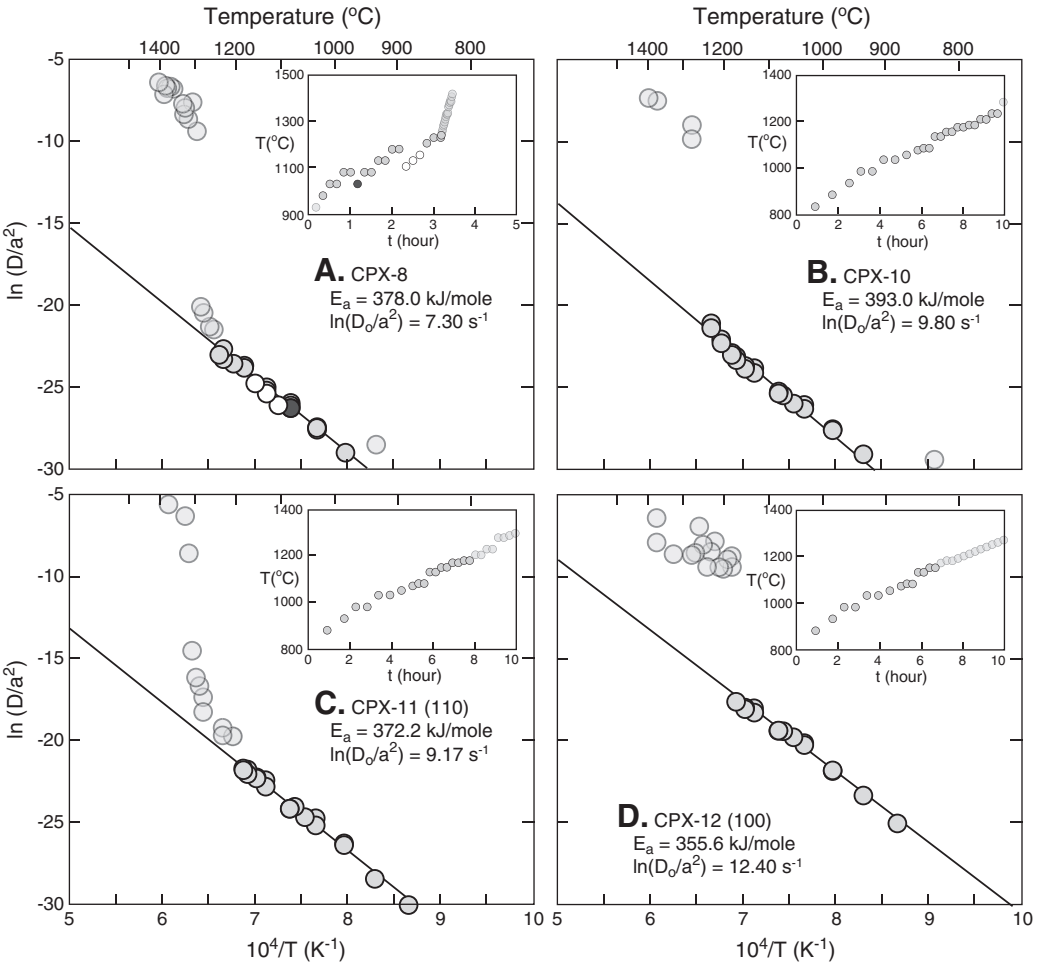

Fig. 2. Arrhenius plots for (A) CPX-8, (B) CPX-10, (C) CPX-11, and (D) CPX-12. Uncertainties in calculated D/a^2 values are generally smaller than the symbols, but are not shown. The laboratory heating schedules are shown in the insets. Data corresponding to lighter symbols were not included in E_a and $\ln(D_o/a^2)$ calculations. CPX-8 was subjected to cycled heating, denoted by varied data colors.

same microstructural characteristics. Thus differences in the cumulative fraction of ^{37}Ar degassed prior to departures from linear Arrhenius arrays likely reflect variations in crystal size and heating schedule (discussed below), not microstructural differences.

Upward curvature observed on the Arrhenius plots is strongly dependent on extraction temperature and generally occurs between 1225 and 1300 °C for CPX. Greater than 90% of the remaining ^{37}Ar contained within each CPX crystal is released in a single extraction step in this temperature range. This "argon bursting" is manifest as a large upward excursion on Arrhenius plots (Figs. 1 and 2). Reducing the duration and increasing the number of extractions between 1200 and 1350 °C (e.g., 60 s at 10 degree increments as opposed to 600 s at 50 degree increments) yields Arrhenius arrays that curve more smoothly upward prior to bursting (e.g., Figs. 2A, 5B, C). Extensively increasing the duration of heating at temperature just below 1250 °C appears to cause upward curvature at lower temperatures (as low as 1180 °C; Figs. 2C, D and 5B, C). Cycled heating to lower temperatures following heating to 1250 °C does not yield D/a^2 values consistent with prior extractions at the same temperature (e.g., Fig. 1A and C). This observation, along with the time- and temperature-dependence, suggests that the data reflect an irreversible, progressive structural change that enhances Ar diffusion (see discussion section). Bursting occurs at slightly higher temperature for OPX (1377 to 1425 °C), which likely reflects OPX's higher melting temperature.

To assess whether the physical crystal fragment represents the diffusion domain boundary, we analyzed several different sizes of CPX and OPX crystals. Because the CaO concentration in each CPX (or each OPX) crystal fragment is uniform in these homogenous pyroxenes, the total ^{37}Ar abundance in each sample is an excellent proxy for crystal volume. Therefore, we can approximate the diffusive lengthscale a using the total ^{37}Ar abundance, spectrometer sensitivity, Ca concentration, and an irradiation parameter that relates ^{37}Ar to grams of Ca (see the supplementary files for calculation details). A negative correlation between $\ln(D_o/a^2)$ and a is expected if (1) D_o is constant, (2) the crystal fragment defines the diffusion domain, (3) the crystal fragments have similar aspect ratios to each other and are regressed using analytical solutions for the same geometry, and (4) diffusion is isotropic. By inspection of Fig. 6 it is evident that CPX and OPX $\ln(D_o/a^2)$ values correlate inversely with crystal size, indicating that the range in observed $\ln(D_o/a^2)$ values likely results from grain size variations and therefore that the physical crystal fragment defines the diffusion domain in these gem-quality, fracture-free crystal fragments. As noted above, larger grains (>1 mm) generally yielded non-linear Arrhenius arrays typical of material containing multiple diffusive length-scales (Fig. 5). Thus it appears likely that intra-grain cleavage planes or fractures (rather than the physical crystal dimensions) may define the diffusion lengthscale of large (>1 mm) pyroxenes. As such, the E_a reported in Table 2 is likely a good reference for fitting more complex, non-linear Arrhenius arrays obtained from larger natural pyroxenes with a multi-domain model (e.g., Cassata et al., 2010; Lovera et al., 1991).

We determined D_o from D_o/a^2 using those OPX and CPX fragments for which we measured the dimensions under a binocular microscope (images and measurements appear in the supplementary files). For the

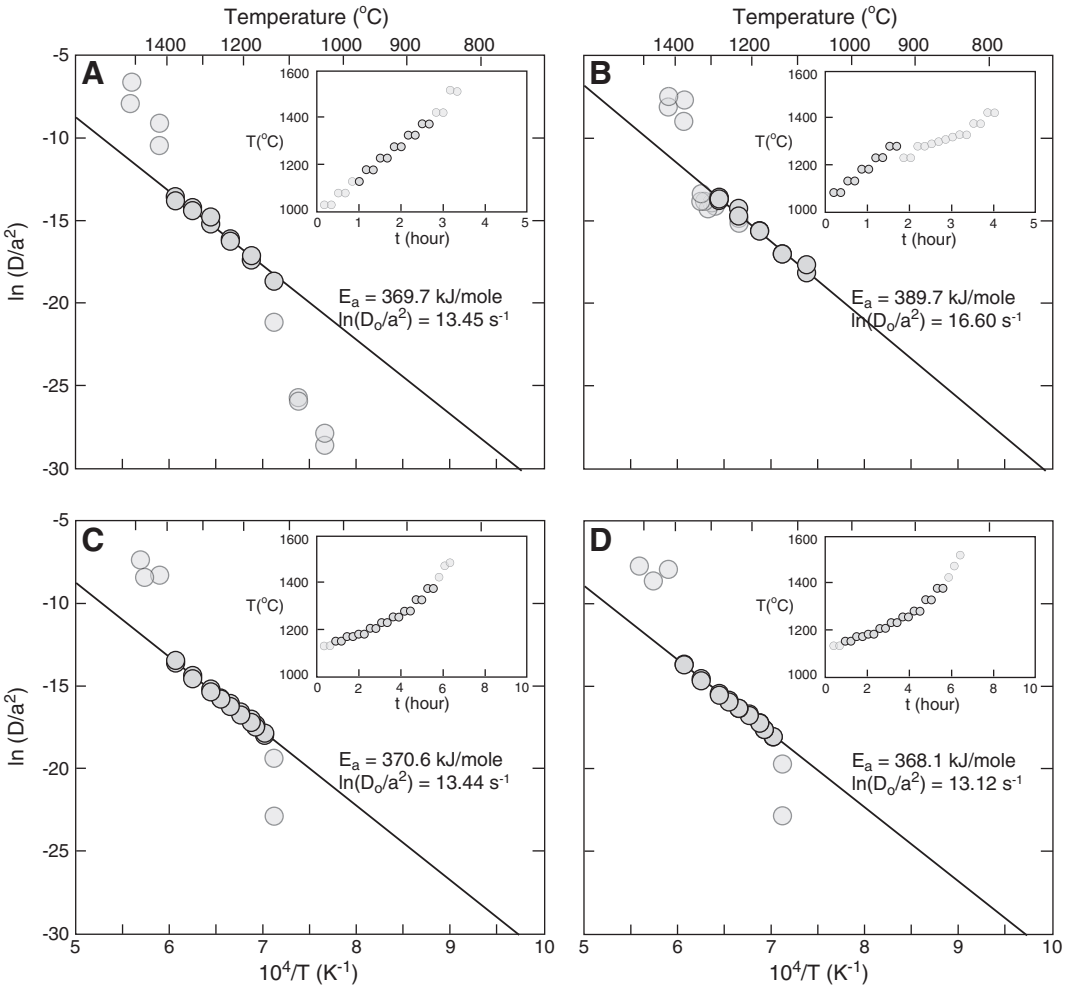

Fig. 3. Arrhenius plots for (A) OPX-1, (B) OPX-3, (C) OPX-4, and (D) OPX-5. Uncertainties in calculated D/a^2 values are generally smaller than the symbols, but are not shown. The laboratory heating schedules are shown in the insets. Data corresponding to lighter symbols were not included in E_a and $\ln(D_o/a^2)$ calculations.

oriented CPX sheets, the relevant diffusion dimension (a) for infinite sheet geometry is half of the total thicknesses normal to the {110} and {100} crystal faces. For the bulk CPX and OPX crystals, the relevant

Table 2
Summary of diffusion parameters.

Sample	MSWD	n Included	% ^{37}Ar Included	$E_a \pm 1\sigma$ (kJ/mole)	$\ln(D_o/a^2) \pm 1\sigma$ ($\ln(s^{-1})$)
CPX-1	1.90	0.73	0.73	386.4 ± 11.6	8.0 ± 1.0
CPX-3	1.70	0.22	0.22	376.4 ± 14.9	8.2 ± 1.3
CPX-4	1.20	0.95	0.95	391.3 ± 12.0	11.0 ± 1.0
CPX-5	1.09	0.17	0.17	386.4 ± 11.2	7.2 ± 1.9
CPX-6	1.80	0.21	0.21	393.8 ± 17.4	9.2 ± 1.5
CPX-8	0.29	0.17	0.17	378.0 ± 19.5	7.3 ± 1.7
CPX-9	0.77	0.18	0.18	373.9 ± 21.6	7.2 ± 1.7
CPX-10	2.50	0.52	0.52	393.0 ± 14.6	9.8 ± 1.3
CPX-11[a] {110}	1.11	0.17	0.17	372.2 ± 9.5	9.2 ± 0.9
CPX-12[a] {100}	0.91	0.97	0.97	355.6 ± 10.8	12.4 ± 1.0
			Wtd. Ave.	**379.2 ± 4.1**	
OPX-1	1.80	17.17	17.17	369.7 ± 22.8	13.5 ± 1.8
OPX-3	1.80	15.89	15.89	389.7 ± 20.0	16.6 ± 1.6
OPX-4	1.60	22.27	22.27	370.6 ± 9.1	13.4 ± 0.7
OPX-5	0.80	20.88	20.88	368.1 ± 9.1	13.1 ± 0.7
			Wtd. Ave.	**371.0 ± 6.0**	

Diffusion parameters determined using analytical solutions for spherical geometry, unless otherwise noted.
[a] Diffusion parameters for oriented sheets determined using infinite sheet geometry.

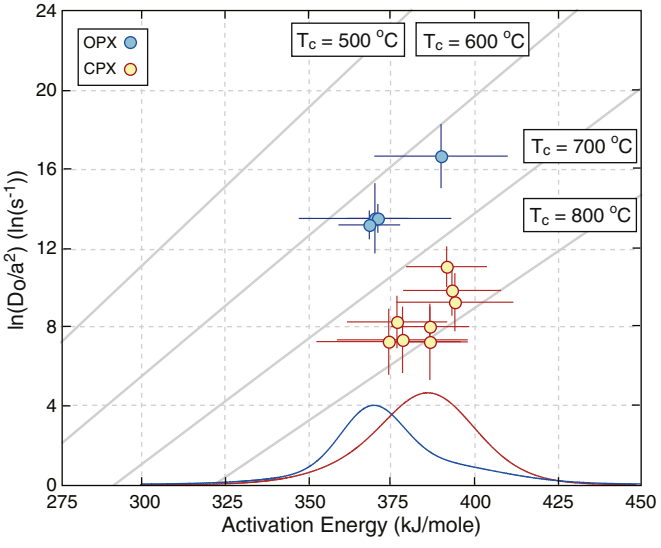

Fig. 4. Summary of kinetic parameters for diffusion of ^{37}Ar in clinopyroxene (red) and orthopyroxene (blue). Lines correspond to closure temperatures (Dodson, 1973) between 500 and 800 °C, calculated for a 10 °C/Ma cooling.

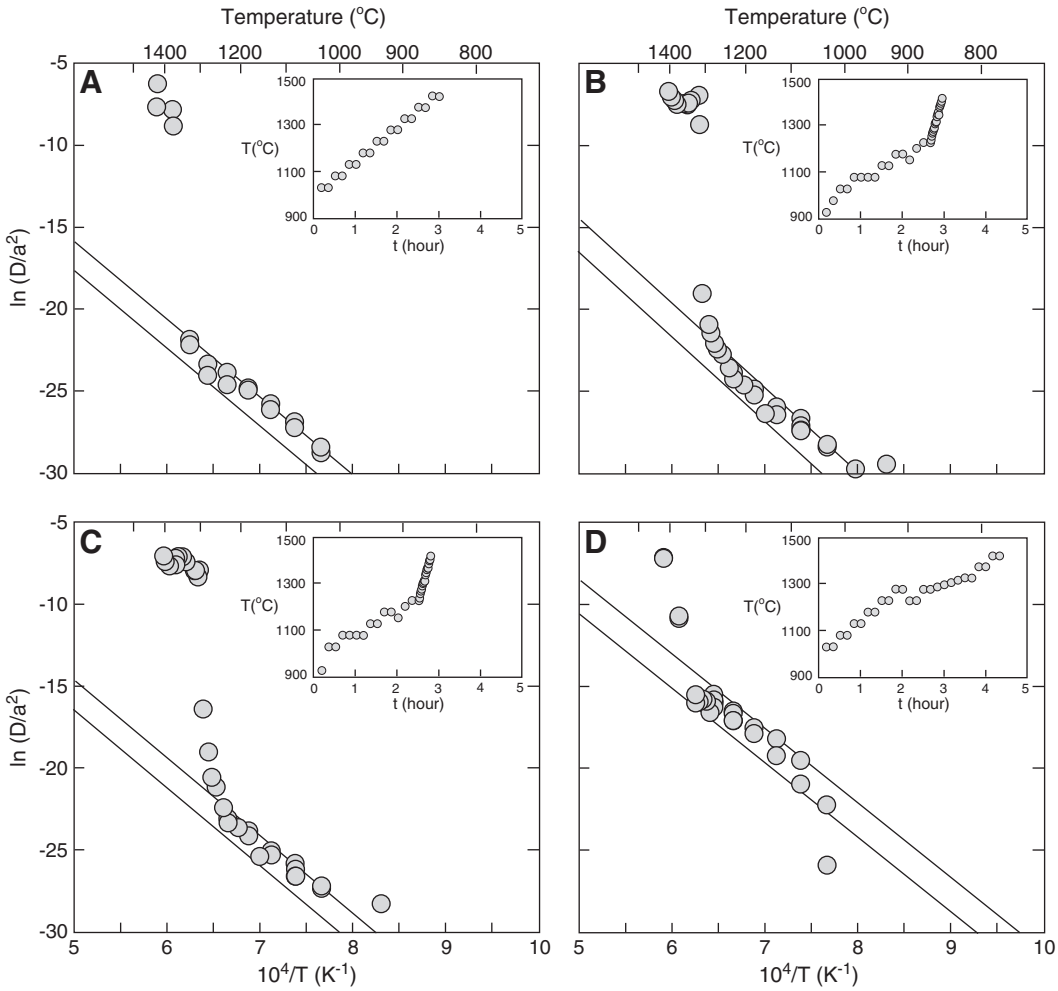

Fig. 5. Arrhenius plots for (A) CPX-2, (B) CPX-7, (C) CPX-13, and (D) OPX-2. Uncertainties in calculated D/a^2 values are generally smaller than the symbols, but are not shown. The laboratory heating schedules are shown in the insets. These samples yielded non-linear Arrhenius arrays typical of crystals with multiple diffusion domains.

diffusion dimension for spherical geometry is the spherical equivalent radius [i.e., the radius of a sphere that diffuses at the same rate as the tetragonal prism (pyroxene crystal) of interest]. We calculated the spherical equivalent radius using the average normalized distance (AND) approach described in Huber et al. (2011) for tetragonal prisms of dimensions $2x \cdot 2y \cdot 2z$. Calculated D_o values are summarized in Table 3. Both un-oriented OPX fragments yield indistinguishable D_o (Table 3). Similarly, the thin CPX sheets intended to isolate diffusion normal to the {110} and {100} crystal faces, as well as the bulk CPX grain that includes diffusion normal to the {001} lattice plane (i.e., along the c-axis), yield statistically indistinguishable D_o at 2σ (Table 3), although the precision permits over an order of magnitude variation (i.e., a factor of ten difference in D_o is not resolvable). More extensive experiments are required to thoroughly test for resolvable diffusive anisotropy.

To summarize, argon diffusivity in CPX and OPX is constrained by the following Arrhenius relationships:

$$\text{CPX}: D_{Ar} = \left(1.36 \times 10^{-4}\right)^{+\,1.12 \times 10^{-4}}_{-6.15 \times 10^{-5}} e\left(\frac{-(379.2 \pm 4.1) kJ/mole}{RT}\right)$$

$$\text{OPX}: D_{Ar} = \left(5.73 \times 10^{-2}\right)^{+\,3.72 \times 10^{-2}}_{-2.25 \times 10^{-2}} e\left(\frac{-(371.0 \pm 6.0) kJ/mole}{RT}\right).$$

In smaller pyroxene crystals (<1 mm), the physical crystal fragment defines the diffusion domain in our experiments. Larger pyroxenes (>1 mm) appear to comprise multiple diffusion domains. At temperatures above ~1225 or 1350 °C for CPX and OPX, respectively, the Arrhenius arrays curve sharply upward, which likely reflects a progressive structural change that enhances Ar diffusion (see Discussion section).

5. Discussion

5.1. Implications for thermochronometry

5.1.1. Slow cooling

Based on the linear Arrhenius arrays between 850 and 1350 °C (Figs. 1 and 2), we calculate closure temperatures (Dodson, 1973) of 600–700 and 700–800 °C for OPX and CPX, respectively, for 10 °C/Ma cooling. The results suggest that at temperatures below ~800 °C pyroxenes are more retentive of Ar than comparably sized glass, feldspars, amphibole, and micas (e.g., from data compiled by Zhang, 2008; Baxter, 2010), and therefore may constrain higher-temperature portions of thermal histories. Examples in the literature of pyroxenes that yield older $^{40}Ar/^{39}Ar$ ages than co-genetic glass and/or feldspars are abundant (e.g., partially reset meteorites; Bogard et al., 1995; Kunz et al., 1997). We are only aware of one $^{40}Ar/^{39}Ar$ study that attempted to compare a pyroxene age to that of co-genetic muscovite, but the muscovite was found to have excess Ar and yielded an anomalously old age (Wang et al., 2000). Similarly, we are only aware of one $^{40}Ar/^{39}Ar$ study that compared pyroxene and amphibole ages:

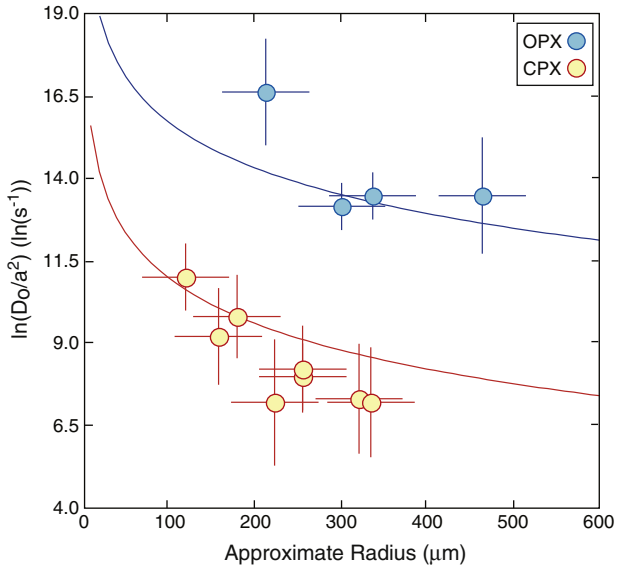

Fig. 6. Plot of approximate diffusion lengthscale versus $\ln(D_o/a^2)$ (see the supplementary files for an example calculation; CPX-11 and CPX-12 not shown). If each CPX and OPX crystal is characterized by the same D_o and differences in $\ln(D_o/a^2)$ values are only due to grain size variations, we expect data to plot on the red and blue lines, respectively. These lines simply represent $\ln(D_o/a^2)$ values expected for a constant D_o and variable a defined by the x-axis. D_o for CPX is that of CPX-10 and for OPX is the weighted average of OPX-4 and OPX-5 (Table 3). Since the observations are in reasonable agreement with these relationships, it appears that grain size variations account for at least most of the observed variance in $\ln(D_o/a^2)$ values and therefore that the physical crystal dimensions define the diffusion domain boundaries. Some scatter about the trend likely results from variations in the aspect ratios of different crystals, which affect $\ln(D_o/a^2)$ values obtained from Arrhenius plots calculated using analytical solutions for spherical geometry.

Haiqing et al. (1996) found that pyroxene, amphibole, and plagioclase from Taipingzhai granulites in China yield plateau ages of 2179 ± 39, 1990 ± 22, and 1651 ± 25 Ma, respectively, which provides additional evidence that pyroxene is more retentive of Ar than amphibole and plagioclase under common crustal conditions.

5.1.2. Brief, high temperature phenomena and "argon bursting"

$^{40}Ar/^{39}Ar$ age spectra obtained from bulk analyses of extraterrestrial rocks commonly comprise both a low-T segment (generally attributed to a lower Ca/K phase such as plagioclase, K-feldspar, glass, or maskelynite) and a high-T segment (generally attributed to a higher Ca/K phase such as OPX or CPX). Fig. 7 illustrates four such whole-rock age spectra taken from the literature. Shock heating associated with impact events is thought to partially, and in some instances completely, reset the K-Ar system within feldspars and glass owing to the relative ease with which argon diffuses from these phases (see, e.g., low Ca/K portion of age spectra in Figs. 7A and B). Pyroxenes often appear to retain $^{40}Ar^*$ that accumulated prior to impact heating (see, e.g., high Ca/K portion of age spectra in Fig. 7A

Table 3
Summary of D_o calculations.

Sample	Diffusion Lengthscale (μm)	$\ln(D_o) \pm 1\sigma$ ($\ln(m^2\ s^{-1})$)
CPX-10	180.0	−7.44 ± 1.25
CPX-11 {110}	64.5	−10.13 ± 0.85
CPX-12 {100}	32.9	−8.24 ± 1.00
	Wtd. Ave.	−8.90 ± 0.60
OPX-4	312.0	−2.71 ± 0.70
OPX-5	314.0	−3.01 ± 0.70
	Wtd. Ave.	−2.86 ± 0.50

CPX $D_o = 1.36E\text{-}04^{+1.12E\text{-}04}_{-6.15E\text{-}05}$
OPX $D_o = 5.73E\text{-}02^{+3.72E\text{-}02}_{-2.25E\text{-}02}$

Approximate diffusion lengthscales for CPX-11 and CPX-12 are the slab half-widths and $\ln(D_o)$ was calculated assuming infinite sheet geometry.
Approximate diffusion lengthscales for CPX-10, OPX-4, and OPX-5 are the spherical equivalent radii calculated using the AND approach (see text for description) and $\ln(D_o)$ was calculated assuming spherical geometry.
Images of each crystal are given in the supplementary files.

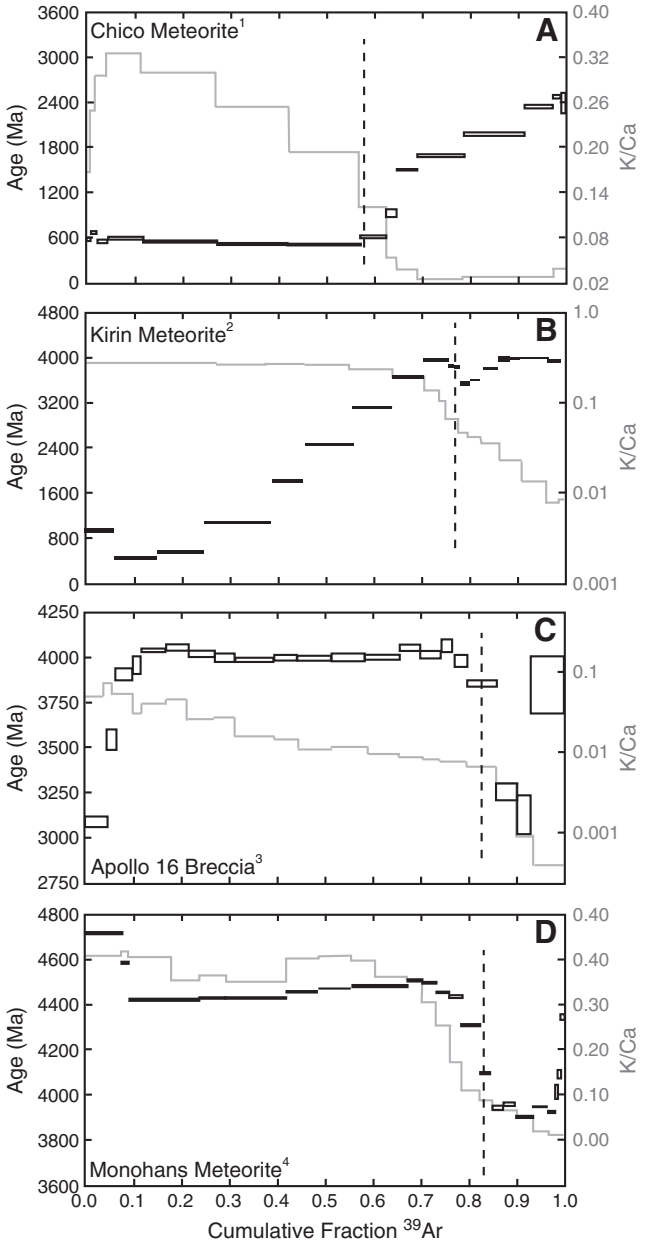

Fig. 7. Apparent age and K/Ca spectra for various meteorites plotted against the cumulative fraction of ^{39}Ar. Pyroxene-derived data lie to the right of the dashed lines and are distinguished by low K/Ca ratios. Feldspar- and/or glass-derived data lie to the left of the dashed lines and are distinguished by higher K/Ca ratios. Data near the dashed line likely contain contributions from feldspar and/or glass and pyroxene. These four samples illustrate the range of age spectra that result from resetting of the K-Ar system in multiphase meteorites by impact heating, including (A) extensive resetting of feldspar and/or glass and minor resetting of pyroxene, (B) moderate resetting of feldspar and/or glass and minor resetting of pyroxene, (C) moderate resetting of feldspar and/or glass and pyroxene, and (D) moderate to extensive resetting of pyroxene and only minor resetting of feldspar and/or glass. Data re-drafted from (A) Bogard et al. (1995), (B) Wang et al. (1980), (C) Jessberger et al. (1974), and (D) Bogard et al. (2001).

and B), presumably reflecting lower Ar diffusivity in pyroxenes and therefore less $^{40}Ar^*$ loss during the heating event. However, in some instances pyroxene-derived segments of whole rock age spectra define diffusive loss profiles with ages that are significantly younger than some or all feldspar/glass-derived ages. Observations of this feature fall into three broad categories: (1) those in which the pyroxene portion of the age spectra appears less discordant than the feldspar/glass portion (e.g., Fig. 7B), (2) those in which feldspar/glass and pyroxene portions of the age spectra are equivalently discordant (e.g., Fig. 7C), and (3) those in which pyroxene portion of the age spectra appears more discordant than the feldspar/glass portion (e.g., Fig. 7D). With few exceptions (e.g., Wang et al., 1980), pyroxene ages that appear spuriously young have been ascribed to recoil-implanted ^{39}Ar from a potassium (K)-rich donor phase (e.g., Huneke and Smith, 1976; Turner and Cadogan, 1974), rather than diffusive loss from pyroxene. It stood to reason that if the discordance observed in the pyroxene portion of the age spectrum was a diffusive phenomenon, then the underlying heating event would have extensively degassed the feldspars/glass (e.g., Chico meteorite; Fig. 7A; Bogard et al., 1995).

On the basis of mineralogy and grain size distributions, Cassata et al. (2010) suggested that ^{39}Ar recoil may not be an adequate explanation for age discordance observed in some of these meteorites and that the data may reflect diffusive distributions of $^{40}Ar^*$. They hypothesized that, because of the strong temperature dependence of Ar diffusion in pyroxenes, Ar loss may proceed more rapidly from pyroxenes than it does from feldspars or glasses at high temperatures relevant to shock events. The diffusion kinetics determined in the present study provide validation for the inferences by Cassata et al. (2010) and indicate that $^{40}Ar/^{39}Ar$ data from pyroxenes likely hold potential for resolving unusually brief, high-temperature phenomena such as impact events. Subsequent low-T heating should minimally obscure these features.

It should be emphasized that there are still several issues to be considered (see discussion in Cassata et al., 2010). It is not clear from this study whether the diffusion kinetics quantified between 850 and 1350 °C can be extrapolated to higher temperatures relevant to shock events. If argon "bursting" observed during laboratory heating between 1225 and 1400 °C occurs in nature, then Ar diffusion at shock temperatures may be substantially more rapid than is predicted by upward extrapolation of the Arrhenius arrays quantified in this study. For this reason, it is important to understand the underlying cause of argon bursting in pyroxenes. It is possible that bursting simply reflects extensive fracturing in response to thermal stresses associated with stepped-heating, thereby drastically reducing the diffusive lengthscale. However, SEM images of a CPX crystal that was heated to 1300 °C do not reveal obvious fracturing (see supplementary files for images). We suggest instead that argon bursting is a result of early partial melting (EPM) and disordering of the cationic sublattice (Doukhan et al., 1993). EPM is the exsolution of a molten phase enriched in SiO_2 occurring below the melting temperature (Doukhan et al., 1993). The onset of extensive EPM in CPX occurs between 1255 and 1323 °C (Doukhan et al., 1993; Richet and Fiquet, 1991; Richet et al., 1994), with minor EPM occurring as low as 1140 °C (Doukhan et al., 1993). This is the same temperature range over which upward curvature is observed on Arrhenius plots for Ar diffusion (Figs. 1 and 2). SEM images of a CPX crystal that was heated to 1300 °C reveal melt-like features on the crystal surface (see supplementary files for images). The onset of EPM in OPX was observed at 1300 °C (Doukhan et al., 1993). Similarly, we observed argon bursting in OPX at temperatures above 1300 °C. Enhanced ion mobility often accompanies (and may be the cause of) pre-melting (Ubbelohde, 1978). For example, Arrhenius plots for Ca diffusion in CPX exhibit drastic upward kinks between 1231 and 1242 °C, the same temperature within uncertainty at which the onset of extensive EPM occurs (Dimanov and Ingrin, 1995; Dimanov and Jaoul, 1998). These inflections are remarkably similar to those observed on Ar Arrhenius plots and occur at the same temperature [compare Figs. 1 and 2 with Fig. 3 in Dimanov and Ingrin (1995) and Fig. 4 in Dimanov and Jaoul (1998)]. Enhanced cation mobility is thought to result from a rapid increase in the density of Frenkel defects along M1 and M2 cation sites as the crystal disorders and octahedrally coordinated M3 and M4 interstitial sites become available to cations (Dimanov and Ingrin, 1995; Dimanov and Jaoul, 1998; Doukhan et al., 1993). A rapid increase in defect density offers a straightforward explanation for argon bursting observed *in vacuo*.

At a given temperature, the extent of EPM correlates inversely with pressure (Doukhan et al., 1993), which likely reflects the fact that the melting temperature of CPX increases with increasing pressure (Yoder, 1952). Thus it is possible that upward curvature (enhanced diffusivity) observed on Arrhenius plots occurs at higher temperatures at pressures relevant to shock events. However, the possible importance of pressure-dependent reductions in high-temperature diffusivity due to activation volume (e.g., Watson and Baxter, 2007) remains to be investigated. The actual diffusion mechanism during ultra-brief shock events at fleetingly high pressures is essentially unknown. Nonetheless, the diffusion parameters in this study should reflect a minimum diffusivity, which may be enhanced at high temperatures by argon bursting.

5.2. Implications for mantle degassing

Our measured diffusion parameters for Ar in pyroxenes differ from those reported by Watson et al. (2007). Because clinopyroxene is expected to be the principal K-bearing phase in a nominally anhydrous upper mantle, Watson et al. (2007) concluded that Ar diffusivity in clinopyroxene at typical upper mantle conditions is sufficiently slow that ambient degassing of radiogenic ^{40}Ar is insignificant. Watson et al. (2007) concluded moreover that during partial melting ^{40}Ar would be partitioned into olivine and orthopyroxene and be sequestered there due to inferred high compatibility of Ar in these phases relative to melts. Watson et al. (2007) proposed on the basis of these premises that mantle degassing is unable to explain the ^{40}Ar content of the atmospheres of Earth and other terrestrial planets.

Our data yield much higher (>10×) activation energies for Ar diffusion in both clinopyroxene and orthopyroxene than was inferred by Watson et al. (2007) for these phases. Assuming a 1 mm diffusion radius, our data indicate diffusivities more than 7 orders of magnitudes higher at temperatures relevant to partial melting of the upper mantle (i.e., ~1300 °C). Previous work on both natural and experimentally grown mineral-melt pairs (e.g., Brooker et al., 2003; Chamorro et al., 2002; Heber et al., 2004, 2007; Hiyagon and Ozima, 1982, 1986; Valbracht et al., 1994) indicates that Ar is highly incompatible in pyroxene. Although some studies were plagued by complications from Ar-rich melt inclusions in crystal phases, mineral-melt partition coefficients of 0.001 were determined by Heber et al. (2007) from carefully documented, inclusion-free olivine and clinopyroxene. Assuming Ar is not compatible in pyroxene or nearby phases, the much higher diffusivities that we measured would ensure continuous degassing and negligible steady-state accumulation of radiogenic Ar in pyroxenes unless the zero surface concentration boundary condition is violated (e.g., Baxter et al., 2002) by high intergranular Ar pressure.

Our results suggest that the low Ar diffusivities in pyroxenes at mantle temperatures reported by Watson et al. (2007) may not reflect bulk pyroxene properties. It is possible that the results reported by Watson et al. (2007) reflect an enhanced region of Ar solubility and/or diminished diffusivity that is surface-correlated, and that the kinetics and solubilities of Ar in an outer, near-surface region are fundamentally distinct from volume-integrated properties. Such a distinction between near-surface and volume-intensive kinetics has also been noted in quartz (Clay et al., 2010) and alkali feldspar (Wartho et al., 1999). Whether the distinct surficial behavior of Ar in these and possibly other minerals is reflected in nature or is induced experimentally remains to be seen and warrants further investigation. In either case, the surficial results in isolation may yield a distorted

view of Ar transport and sequestration in nature. It is also possible that the diffusion parameters reported by Watson et al. (2007) using Rutherford backscattering (RBS) reflect a diffusion mechanism that operates on a very short lengthscale (i.e., pure lattice diffusion) and therefore does not limit the rate of diffusive transport in the bulk crystal, which entails diffusion through the lattice, point defects, planar defects, etc. (i.e., $(Dt/a^2)_{RBS} > (Dt/a^2)_{BULK}$).

6. Conclusions

Diffusion experiments on gem-quality pyroxenes produced highly linear, reproducible Arrhenius arrays between 850 and 1350 °C. CPX grains yield an average E_a of 379.2 ± 4.1 kJ/mol (90.6 ± 1.0 kcal/mol) and D_o of $(1.36\times10^{-4})^{+1.12\times10^{-4}}_{-6.15\times10^{-5}}$. OPX grains yield an average E_a of 371.0 ± 6.0 kJ/mol (88.7 ± 1.4 kcal/mol) and D_o of $(5.73\times10^{-2})^{+3.72\times10^{-2}}_{-2.25\times10^{-2}}$. These data suggests that the K–Ar system in pyroxenes can be used as a thermochronometer in cases wherein their age and K contents, and resolvability of possible excess ^{40}Ar, permit determination of acceptably precise and accurate ^{40}Ar/^{39}Ar ages. Pyroxenes appear to be more retentive of Ar than comparably sized amphibole, biotite, and muscovite grains, and yield closure temperatures of 600–800 °C for a 10 °C/Ma cooling rate and ~0.1–1 mm grain size. Due to the strong temperature dependence of Ar diffusion in pyroxenes, brief, high-temperature shock heating events may extensively degas pyroxene, but low-T phenomena will have little effect on Ar concentration gradients. As such, diffusive ^{40}Ar distributions observed within pyroxenes in meteorites can retain critical information about the timing and nature of shock events on meteorites and their parent bodies. Further study of the crystal-chemical basis for argon bursting and the pressure-dependence of Ar diffusion in pyroxenes would be productive. Our data indicate that radiogenic ^{40}Ar should be degassed rapidly from Earth's mantle during partial melting events.

Acknowledgements

The authors acknowledge financial support from the NSF Petrology and Geochemistry program (grant EAR-0838572 to P.R.R. and D.L.S.) and the Ann and Gordon Getty Foundation. T. Becker is thanked for assistance in the Ar lab. W.S. Cassata was supported by a National Science Foundation Graduate Research Fellowship. J. Kula and O. Lovera are thanked for thoughtful and constructive reviews. Becky Smith is thanked for orienting CPX crystal fragments using the SEM, and J. Donovan is thanked for the electron microprobe analyses.

Appendix A. Supplementary data

Supplementary data to this article can be found online at doi:10.1016/j.epsl.2011.02.019.

References

Amirkhanov, K.H.I., Bartnitzkii, E.N., Brandt, S.B., Voitkevich, G.V., 1959. The migration of aragon and helium in certain rocks and minerals. Geochemistry Series Dokl. Acad. Sci. USSR 126.

Baxter, E.F., DePaolo, D.J., Renne, P.R., 2002. Spatially correlated anomalous ^{40}Ar/^{39}Ar. Geochim. Cosmochim. Acta 66, 1067–1083.

Bogard, D.D., Garrison, D.H., Norman, M., Scott, E.R.D, Keil, K., 1995. ^{39}Ar–^{40}Ar age and petrology of Chico: large-scale impact melting on the L chondrite parent body. Geochim. Cosmochim. Acta 59, 1383–1399.

Bogard, D.D., Garrison, D.H., Masarik, J., 2001. The Monahans chrondrite and halite: Argon-39/argon-40 age, solar gases, cosmic-ray exposure ages, and parent body regolith neutron flux and thickness. Meteoritics and Planetary Science 36, 107–122.

Brooker, R.A., Du, Z., Blundy, J.A., Kelley, S.P., Allan, N.L., Wood, B.J., Chamorro, E.M., Wartho, J.A., Purton, J.A., 2003. The ëzero chargeípartitioning behaviour of noble gases during mantle melting. Nature 423, 738–741.

Brownlee, S.J., Renne, P.R., 2010. Thermal history of the Ecstall pluton from ^{40}Ar/^{39}Ar geochronology and thermal modeling. Geochim. Cosmochim. Acta 74, 4375–4391.

Burgess, R., Turner, G., Laurenzi, M., Harris, J.W., 1989. ^{40}Ar–^{39}Ar laser probe dating of individual clinopyroxene inclusions in Premier eclogitic diamonds. Earth Planet. Sci. Lett. 94, 22–28.

Cassata, W.S., Renne, P.R., Shuster, D.L., 2009. Argon diffusion in plagioclase and implications for thermochronometry: a case study from the Bushveld Complex, South Africa. Geochim. Cosmochim. Acta 73, 6600–6612.

Cassata, W.S., Shuster, D.L., Renne, P.R., Weiss, B.P., 2010. Evidence for shock heating and constraints on Martian surface temperatures revealed by ^{40}Ar/^{39}Ar thermochronometry of Martian meteorites. Geochim. Cosmochim. Acta 74, 6900–6920.

Chamorro, E.M., Brooker, R.A., Wartho, J.A., Wood, B.J., Kelley, S.P., Blundy, J.D., 2002. Ar and K partitioning between clinopyroxene and silicate melt to 8 GPa. Geochim. Cosmochim. Acta 66, 507–519.

Clay, P.L., Baxter, E.F., Cherniak, D.J., Kelley, S.P., Thomas, J.B., Watson, E.B., 2010. Two diffusion pathways in quartz: a combined UV-laser and RBS study. Geochim. Cosmochim. Acta 74, 5906–5925.

Crank, J., 1975. The Mathematics of Diffusion. Clarendon Press, Oxford. 414 pp.

Dimanov, A., Ingrin, J., 1995. Premelting and high-temperature diffusion of Ca in synthetic diopside — an increase of the cation mobility. Phys. Chem. Miner. 22, 437–442.

Dimanov, A., Jaoul, O., 1998. Calcium self-diffusion in diopside at high temperature: implications for transport properties. Phys. Chem. Miner. 26, 116–127.

Dodson, M.H., 1973. Closure temperature in cooling geochronological and petrological systems. Contrib. Mineralog. Petrol. 40, 259–274.

Doukhan, N., Doukhan, J.C., Ingrin, J., Jaoul, O., Raterron, P., 1993. Early partial melting in pyroxenes. Am. Mineralog. 78, 1246–1256.

Fechtig, H., Gentner, W., Zahringer, J., 1960. Argon determination in potassium minerals. VII. Diffusion escape of argon in minerals and its effect on the potassium–argon age determination. Geochim. Cosmochim. Acta 19.

Fechtig, H., Kalbitzer, S., 1966. The Diffusion of Argon in Potassium-Bearing Solids. In: Fechtig, H., Kalbitzer, S., Schaeffer, O., Zahringer, J. (Eds.), Potassium–Argon Dating. Springer Verlag, pp. 68–106.

Haiqing, S., Songshan, W., Ji, Q., 1996. The ^{40}Ar–^{39}Ar ages of Pyroxene, Hornblende and Plagioclase in Taipingzhai Granulites in Qianxi County, Hebei Province and their geological implications. Acta Petrol. Sin. 3, 390–400.

Hart, S.R., 1960. Mineral Ages and Metamorphism. Massachusetts Institute of Technology, p. 219.

Heber, V.S., Brooker, R.A., Kelley, S.P., Wood, B.J., 2004. Diffusion behaviour of noble gases in mantle minerals: high resolution UV laser depth profiling. Lithos 73, S49.

Heber, V.S., Brooker, R.A., Kelley, S.P., Wood, B.J., 2007. Crystal-melt partitioning of noble gases (helium, neon, argon, krypton, and xenon) for olivine and clinopyroxene. Geochim. Cosmochim. Acta 71, 1041–1061.

Hiyagon, H., Ozima, M., 1982. Noble gas distribution between basalt melt and crystals. Earth Planet. Sci. Lett. 58, 255–264.

Hiyagon, H., Ozima, M., 1986. Partition of noble gases between olivine and basalt melt. Geochim. Cosmochim. Acta 50, 2045–2057.

Huber, C., Cassata, W.S., Renne, P.R., 2011. A lattice Boltzmann model for noble gas diffusion in solids: The importance of domain shape and diffusive anisotropy and implications for thermochronometry. Geochim. Cosmochim. Acta. doi:10.1016/j.gca.2011.01.039.

Huneke, J.C., Smith, S.P., 1976. The realities of recoil: ^{39}Ar recoil out of small grains and anomalous age patterns in ^{39}Ar–^{40}Ar dating. Proceedings of the 7th Lunar Science Conference. Pergamon Press, pp. 1987–2008.

Jessberger, E.K., Huneke, J.C., Podosek, F.A., Wasserburg, G.J., 1974. High resolution argon analysis of neutron-irradiated Apollo 16 rocks and separated minerals. Proceedings of the Fifth Lunar Conference 2, 1419–1449.

Kohn, M.J., Spear, F.S., Harrison, T.M., Dalziel, I.W.D., 1995. ^{40}Ar/^{39}Ar geochronology and P-T-t paths from the Cordillera Darwin metamorphic complex, Tierra del Fuego, Chile. Journal of Metamorphic geology 13, 251–270.

Kunz, J., Falter, M., Jessberger, E., 1997. Shocked meteorites: ^{40}Ar–^{39}Ar evidence for multiple impacts. Meteorit. Planet. Sci. 32, 647–670.

Lovera, O.M., Richter, F.M., Harrison, T.M., 1991. Diffusion domains determined by ^{39}Ar released during step heating. J. Geophys. Res. 96, 2057–2069.

Phillips, D., Harris, J.W., Kiviets, G.B., 2004. Ar-40/Ar-39 analyses of clinopyroxene inclusions in African diamonds: implications for source ages of detrital diamonds. Geochim. Cosmochim. Acta 68, 151–165.

Phillips, D., Onstott, T.C., Harris, J.W., 1989. Ar-40/Ar-39 laser-probe dating of diamond inclusions from the Premier Kimberlite. Nature 340, 460–462.

Renne, P.R., 2000. ^{40}Ar/^{39}Ar age of plagioclase from Acapulco meteorite and the problem of systematic errors in cosmochronology. Earth Planet. Sci. Lett. 175, 13–26.

Renne, P.R., Schwarcz, H.P., Kleindienst, M.R., Osinski, G.R., Donovan, J.J., 2010. Age of the Dakhleh impact event and implications for Middle Stone Age archeology in the Western Desert of Egypt. Earth Planet. Sci. Lett. 291, 201–206.

Richet, P., Fiquet, G., 1991. High-temperature heat capacity and premelting of minerals in the system MgO–CaO–Al2O3–SiO2. J. Geophys. Res. Solid Earth Planets 96, 445–456.

Richet, P., Ingrin, J., Mysen, B.O., Courtial, P., Gillet, P., 1994. Premelting effects in minerals: an experimental study. Earth Planet. Sci. Lett. 121, 589–600.

Richter, F.M., Lovera, O.M., Harrison, T.M., Copeland, P., 1991. Tibetan tectonics from ^{40}Ar/^{39}Ar analysis of a single K-feldspar sample. Earth Planet. Sci. Lett. 105, 266–278.

Schwartzman, D.W., Giletti, B.J., 1977. Argon diffusion and absorption studies of pyroxenes from the Stillwater complex, Montana. Contrib. Mineralog. Petrol. 60, 143–159.

Shuster, D.L., Balco, G., Cassata, W.S., Fernandes, V.A., Garrick-Bethell, I., Weiss, B.P., 2010. A record of impacts preserved in the lunar regolith. Earth Planet. Sci. Lett. 290, 155–165.

Turner, G., Cadogan, P.H., 1974. Possible effects of ^{39}Ar recoil in ^{40}Ar–^{39}Ar dating. Proceedings of the 5th Lunar Science Conference. Pergamon Press, pp. 1601–1615.

Turner, G., Enright, M.C., Hennessy, J., 1978. Diffusive loss of argon from chondritic meteorites. Meteoritics 13, 648.

Ubbelohde, A.R., 1978. The Molten State of Matter. John Wiley and Sons, New York.

Valbracht, P.J., Honda, M., Staudigel, H., McDougall, I., Trost, A.P., 1994. Noble gas partitioning in natural samples: results from coexisting glass and olivine phenocrysts in four Hawaiian

submarine basalts. Noble Gas Geochemistry and Cosmochemistry. Terra Scientific, Tokyo, pp. 373–381.
Wang, S., Ge, N., Sang, H., Qiu, J., 2000. Genesis of excess argon in phengite and significance of ^{40}Ar–^{39}Ar age spectra for omphacite: a case study on UHP eclogite of South Dabie Terrain, China. Chin. Sci. Bull. 45, 1345–1351.
Wang, S., McDougall, I., Tetley, N., Harrison, T.M., 1980. ^{40}Ar/^{39}Ar age and thermal history of the Kirin chondrite. Earth Planet. Sci. Lett. 49, 117–131.
Wartho, J.A., Kelley, S.P., Brooker, R.A., Carroll, M.R., Villa, I.M., Lee, M.R., 1999. Direct measurement of Ar diffusion profiles in a gem-quality Madagascar K-feldspar using the ultra-violet laser ablation microprobe (UVLAMP). Earth Planet. Sci. Lett. 170, 141–153.
Watson, E.B., Baxter, E.F., 2007. Diffusion in solid-Earth systems. Earth Planet. Sci. Lett. 253, 307–327.
Watson, E.B., Thomas, J.B., Cherniak, D.J., 2007. ^{40}Ar retention in the terrestrial planets. Nature 449, 299–304.
Weirich, J.R., Isachsen, C.E., Johnson, J.R., Swindle, T.D., 2010. Argon diffusion in pyroxene and albite. 41st Lunar and Planetary Science Conference, 2137.
Yoder, H.S., 1952. Change of melting point of diopside with pressure. J. Geol. 60, 364–374.
You, Z., 1997. Geochronology of ^{40}Ar–^{39}Ar of ophiolite complex in Dingqing area, North Tibet China. Tibet Geology 2, 24–30.
Zhang, Y., 2008. Geochemical Kinetics. Princeton University Press.